SEA SURFACE WIND FIELD BY X-BAND TERRASAR-X AND TANDEM-X

Susanne Lehner[(1)], XiaoMing Li[(1)], YongZheng Ren[(2)], and MingXia He[(3)]

[(1)] *Remote Sensing Technology Institute, German Aerospace Center (DLR), Oberpfaffenhofen, 82234, Wessling, Germany. Email: Susanne.Lehner@dlr.de*

[(2)] *Key laboratory of Digital Earth, Center for Earth Observation and Digital Earth, Chinese Academy of Sciences (CEODE, CAS), Beijing, 100094, China*

[(3)]*Ocean Remote Sensing Institute, Ocean University of China, Qingdao,266003, China*

ABSTRACT

In the present study, we present the newly developed Geophysical Model Function (GMF), denoted XMOD2, to retrieve the sea surface wind field from X-band TerraSAR-X/Tandem-X (TS-X/TD-X) data. In contrary to the previous XMOD1, XMOD2 is based on a nonlinear GMF, and moreover it also depicts the difference between upwind and downwind of the sea surface backscatter. By exploiting 371 collocations, the retrieved TS-X/TD-X sea surface wind speed by XMOD2 agrees well with in situ buoy measurements with a bias of 0.39 m/s, an RMSE of 1.52 m/s and a scatter index (SI) of 16.1%. To evaluate the sea surface wind field retrieved from X-band SAR, we conducted a joint campaign in the South China Sea in August, 2011. Examples of sea surface wind field retrieved from the TS-X/TD-X data acquired in the campaign are shown for demonstration.

1. INTRODUCTION

The active spaceborne microwave Scatterometer and Synthetic Aperture Radar (SAR) have provided important marine-meteo parameters of the air-sea interface, particularly the sea surface wind speed and direction in high spatial resolution and global coverage. Spaceborne SAR has a unique advantage to measure the sea surface wind field in spatial resolution higher than 1 km, which is particularly important for coastal zones, where the sea surface wind field often exhibits significant spatial variations caused by coastal orography and man-made objects such as oil platforms and offshore wind turbines.

The general methodology to derive the sea surface wind field from SAR is to apply a Geophysical Model Function (GMF) to the calibrated SAR image using wind direction from external sources or wind streaks visible in SAR imagery. The GMF relates the sea surface backscatter to sea surface wind speed, direction and incidence angle of radar. GMF families, e.g., the widely used CMOD4 [1], CMOD_IFR [2] and CMOD5 [3], were originally developed for the C-band (5.3 GHz) ERS Active Microwave Instrument (AMI) Scatterometer and the Advanced SCATterometer (ASCAT) to derive the sea surface wind field over the large swath of scatterometers.

The CMOD functions are generally written as:

$$\sigma_0 = B_0\left(1 + B_1\cos(\phi) + B_2\cos(2\phi)\right) \qquad (1)$$

where B_0, B_1, and B_2 are functions of incidence angle θ and sea surface wind speed v at 10 m height. Relative direction ϕ is the angle between wind direction φ and radar look direction α, i.e. $\phi = \varphi - \alpha$. The scatterometer like the ERS SCAT has fore, mid-, and aft beams with radar looking directions of 45°, 90º and 135º, respectively. Therefore, in a given node with known incidence angles for the three beams, this configuration generates a triplet sea surface backscatter $\sigma_0\left(\sigma_0^{fore}, \sigma_0^{mid}, \sigma_0^{aft}\right)$ from the three beams which were given in [4] and which are reproduced here for reference.

$$\begin{aligned}
\sigma_0^{fore} &= B_0\left[1 + B_1\left(\sin\varphi - \cos\varphi\right)/\sqrt{2} - B_2\sin 2\varphi\right] \\
\sigma_0^{mid} &= B_0^*\left[1 + B_1^*\sin\varphi + B_2^*\cos 2\varphi\right] \\
\sigma_0^{aft} &= B_0\left[1 + B_1\left(\sin\varphi + \cos\varphi\right)/\sqrt{2} + B_2\sin 2\varphi\right]
\end{aligned} \qquad (2)$$

In a given node, values of B_0, B_1, and B_2 are identical in the fore and aft- beams which have the same incidence angles, while values of these three terms in the mid beam are different and thus they are denoted by asterisks. Equ. (2) indicates that the triplet sea surface backscatter at a given node with known incidence angles for the three beams depends only on wind speed U_{10} and wind direction φ. By collocating large amount of reanalysis sea surface wind field data from the European Centre for Medium-Range Weather Forecasts (ECMWF) with scatterometer measurements, transfer functions in B_0, B_1, and B_2 are consequently derived, as presented in [4].

In contrary to scatterometer, SAR has only one beam, therefore the transfer functions in GMF cannot be resolved by using the triplet collocations shown in (2). Since the ERS/SAR and ENVISAT/ASAR were also operated in C-band, the CMOD functions are adopted to the C-band SAR data to map the sea surface wind field over coastal zones for different applications, e.g. meso-scale wind [5], katabatic wind [6], Bora event [7], coastal upwelling [8], and offshore wind farming [9].

Recently, more attention is being drawn to use TS-X/TD-X and Cosmo-SkyMed data for coastal monitoring as they can provide observations with high spatial resolution. The sea surface wind field retrieval is one of promising applications for SAR oceanography in operational services. Therefore, in the present study, we focus on algorithm development for sea surface wind retrieval from TS-X and TD-X data. Our first attempt for sea surface wind field retrieval from the X-band SAR was to develop a linear GMF, called XMOD1 [10], which was tuned using the SIR-X SAR data.

The paper is organized as follows. First, the methodology to develop XMOD2 for sea surface wind field retrieval from TS-X/TD-X VV polarization data is described. Then, the simulation and validation of the XMOD2 are presented. Section 3 presents two examples of sea surface wind retrieval from TS-X/TD-X data acquired in the South China Sea (SCS) campaign. Conclusions and outlook are given in section 4.

2. DEVELOPMENT OF XMOD2

2.1. Data

The TS-X and TD-X instruments can provide radar backscatter in different modes of Spotlight, Stripmap and ScanSAR modes as well as in multiple combinations of polarisations. In the present study, we focus on using the Stripmap and ScanSAR mode data acquired in VV polarisation to retrieve the sea surface wind field. Stripmap data have a pixel size of 2.5 m and a swath of around 30 km, and the ScanSAR mode can provide measurements in large coverage of 100 km at a pixel size of 8.25 m.

For tuning and validation of the XMOD2, i*n situ* buoy measurements are mainly accessed from the National Data Buoy Center (NDBC), USA and the Integrated Science Data Management (ISDM), Canada. Most anemometers are installed at 5 m height on buoys. Therefore, wind speed measured at different anemometer heights are adjusted to the reference level of 10 m height using a log profile. The continuous wind data of the NDBC buoys are available every 10 minutes, while the wind measurements of the Canadian buoys accessed are available hourly.

TS-X/TD-X acquisitions are spatially and temporally matched up to *in situ* buoy measurements. At the locations of the buoys, subscenes of SAR data with coverage of 2 km × 2 km are extracted. The averaged sea surface backscatter σ_0 and the local incidence angle in the TS-X subscenes are collocated with buoy measurements of wind speed and direction.

After excluding SAR data in which the imaged sea surface is strongly affected by rainfall, oil slicks, coastal upwelling or others that affect homogeneity of the sea surface backscatter, there are 371 collocations of TS-X/TD-X in VV polarization and buoy measurements available.

Wind model data provided by the German Weather Service (DWD) are also collocated to TS-X acquisitions. The sea surface wind field at coarse grids of 0.75° in both latitude and longitude is used to drive the global forecast wave model GSM at the DWD; therefore it is hereafter called the GSM wind model. The scatterometer measurements from QuikSCAT (Seawinds) and ASCAT are assimilated into the model. Additionally, QuikSCAT measurements of wind vectors with a spatial resolution of 12.5 km are used as well to compare with the TS-X retrieved wind field.

2.2. Derivation of the XMOD2 for TS-X

Fig. 1 shows the comparison of sea surface backscatter in X-band SAR with the simulated one using CMOD5. In situ buoy measurements of sea surface wind speed and direction are used as input for CMOD5. The comparison indicates that the sea surface backscatter in X-band is very similar to that in C-band. Therefore, we consider that the model functions in C-band GMFs may be adapted to the X-band SAR data.

The CMOD5 is written as:

$$z(v,\phi,\theta) = B_0{}^p(v,\theta)\left(1+B_1(v,\theta)\cos\phi+B_2(v,\theta)\cos 2\phi\right) \quad (3)$$

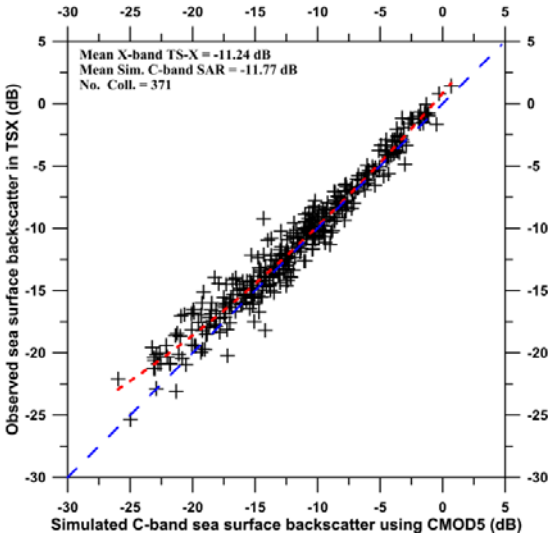

Figure 1. Comparison of the TS-X measurements of σ_0 to the simulated sea surface backscatter using CMOD5.

The sea surface wind speed and direction used in the simulation are derived from the collocated in situ buoy measurements

In which, v, θ and ϕ have the same definition as those given in (1), $p = 0.625$. In CMOD5, the isotropic term B_0, the upwind/downwind amplitude B_1 and upwind/crosswind amplitude B_2 are all the functions of wind speed and incidence angle.

In the GMFs, the isotropic term B_0 and upwind/crosswind amplitude B_2 dominate the relation between sea surface backscatter with wind vector and incidence angle. Therefore, in the proposed GMF XMOD2 for X-band SAR, transfer functions used to depict B_0 and B_2 are adopted from the CMOD5, while a second-order polynomial function is used to describe the dependence of B_1 on the sea surface wind speed and incidence angle as given in (4).

$$B_1 = \sum_{j=0}^{2} \sum_{i=0}^{2} a_{ij} \theta^i v^j \qquad (4)$$

The detailed tuning approaching, as well as the tuned coefficients of transfer functions in XMOD2 are given in [11].

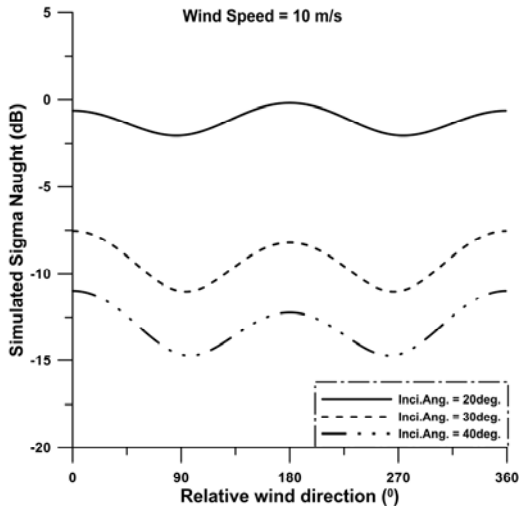

Figure 2. Simulated sea surface backscatter in X-band SAR using the XMOD2 for incidence angles of 20°, 30° and 40° against the relative sea surface wind direction in the sea surface wind speed of 10m/s.

Fig. 2 shows the simulated σ_0 for X-band TS-X using the XMOD2 for incidence angles of 20°, 30° and 40° against the relative sea surface wind direction. The simulation shows that the XMOD2 can represent properly the anisotropic effect of wind direction on the sea surface backscatter. Moreover, the incidence angle effect on the difference between upwind and crosswind, as well as on the difference between upwind and downwind, are also distinct. One can find that the higher incidence angle, the more sensitive σ_0 is on the sea surface wind direction.

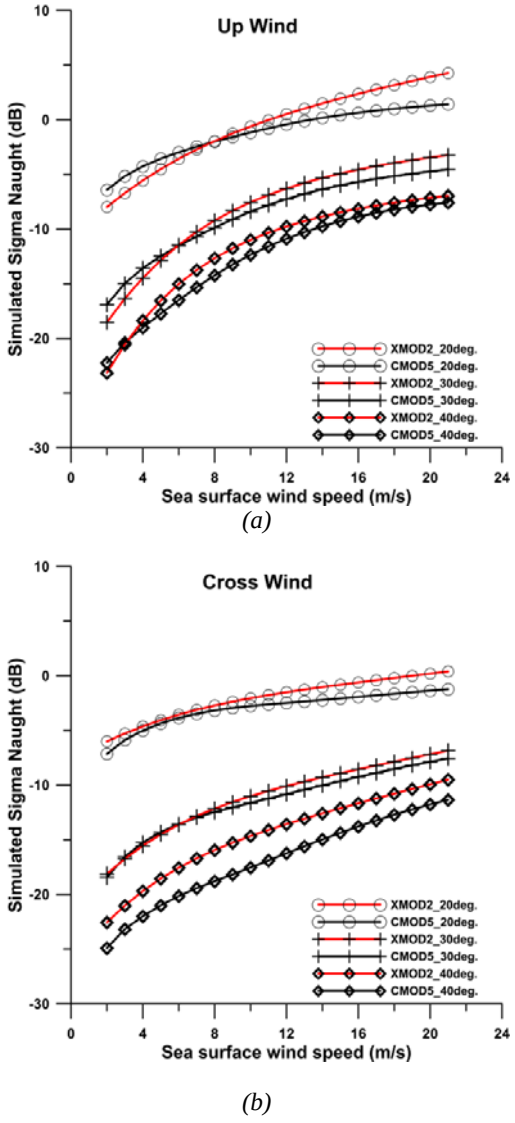

Figure 3. Simulated σ_0 in X-band SAR using the XMOD2 for incidence angles of 20°, 30° and 40° against the sea surface wind speed in upwind (a) and crosswind (b) , as represented by black lines. The red lines show the simulation of σ_0 in C-band SAR using the CMOD5 for comparison.

Fig. 3 (a) and (b) show the simulated sea surface backscatter using XMOD2 for incidence angles of 20°, 30° and 40° in upwind and cross wind situations. The same simulations but using the CMOD5 are also

presented for comparison. It is interesting to notice that, for upwind, the transition of the difference between X-band and C-band σ_0 shows a dependence on incidence angle. For incidence of 20°, 30°, and 40°, the transition appears at around 8 m/s, 6 m/s and 4 m/s, respectively.

Following simulation of XMOD2, we present validation of the newly developed GMF to retrieve sea surface wind field from X-band SAR.

Fig. 4 shows comparison of the retrieved sea surface wind speed using XMOD2 with in situ buoy measurements. The retrieved wind speed is in good agreement with buoy measurements with a bias of 0.39 m/s, an RMSE of 1.52 m/s and a Scatter Index (SI) of 16.3%. The comparison shows that XMOD2 performs well to retrieve the sea surface wind speed in range of 2 m/s and 20 m/s. To further validate the performance of XMOD2, a stepwise comparison along with buoy measurements of wind speed is conducted.

We further match up the TS-X acquisitions with scatterometer measurements of QuikSCAT. By matching up the 409 scenes of TS-X in ScanSAR and Stripmap mode acquired between 2007 (start of TS-X) and 2009 (end of QuikSCAT) with acquisitions of the QuikSCAT, ten cases are available when a temporal window of 1 hour and a spatial distance of 50 km are used. If the temporal window is further reduced to less than 20 minutes which is also used in the studies of [12] and [13] for systematic comparison of the retrieved SAR wind speed with scatterometer measurements, only three cases are left, as listed in Tab.2. As the available collocations with QuikSCAT are too few to derive a scatter diagram like the one shown in Fig. 4, the comparison with QuikSCAT measurements is presented in case studies.

For the three cases, one case is for the TS-X data in ScanSAR mode, and the other two are in Stripmap mode. Here, we present one Stripmap case over the East China Sea which shows a strong winter monsoon wind field. In Fig. 5 (a), the calibrated TS-X image with superimposed QuikSCAT wind field is shown. Measured sea surface wind speed of the QuikSCAT varies between 12 m/s and 15 m/s in the coverage of the TS-X, showing that wind blows homogeneously from northeast to southwest in the China Seas.

Considering that the swath of the TS-X Stripmap data is only around 30 km, the retrieved wind field with a high spatial resolution of 250 m is shown in Fig. 5 (b). As the same colour scale for sea surface wind speed is used in Fig. 5 (a) and (b), one can find the coloured arrows representing the QuikSCAT measurements are nearly invisible in Fig. 5 (b). This indicates that the retrieved TS-X wind speed agrees very well with the QuikSCAT measurements. Further, one can find that the retrieved TS-X wind field also shows some spatial variations. The sea surface wind speed increases gradually from about 10 m/s in the upper left region to above 15 m/s in the lower right one, as the upper left area is nearer to the coastal zone.

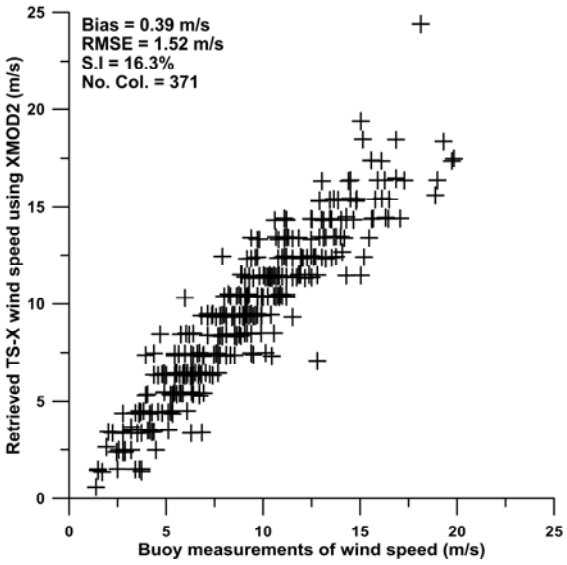

Figure 4 Comparison of the retrieved TS-X/TD-X U_{10} using the XMOD2 against in situ buoy measurements. Buoy measurements of the sea surface wind direction is used as input for the retrieval.

Table 1 List of the TS-X collocation with QuikSCAT between 2007 and 2009

No.	TS-X Time	TS-X Mode	TS-X Location	QSCAT Time	Remark
1	2008-08-25 16:38 UTC	SC	Coast of South Africa, 33°S – 34.5°S/27.5°E - 29°E	2008-08-2516:32 UTC	Strong sea surface wind field
2	2009-02-25 09:51 UTC	SM	Near to Shanghai, China, 28°N – 28.5°N/121.75°E – 122.5°E	2009-02-25 09:52 UTC	winter Monsoon
3	2008-10-20 10:16 UTC	SM	Near to Hongkong, China 22°N – 22.5°N/115°E – 115.5°E	2008-10-20 10:19 UTC	N/A

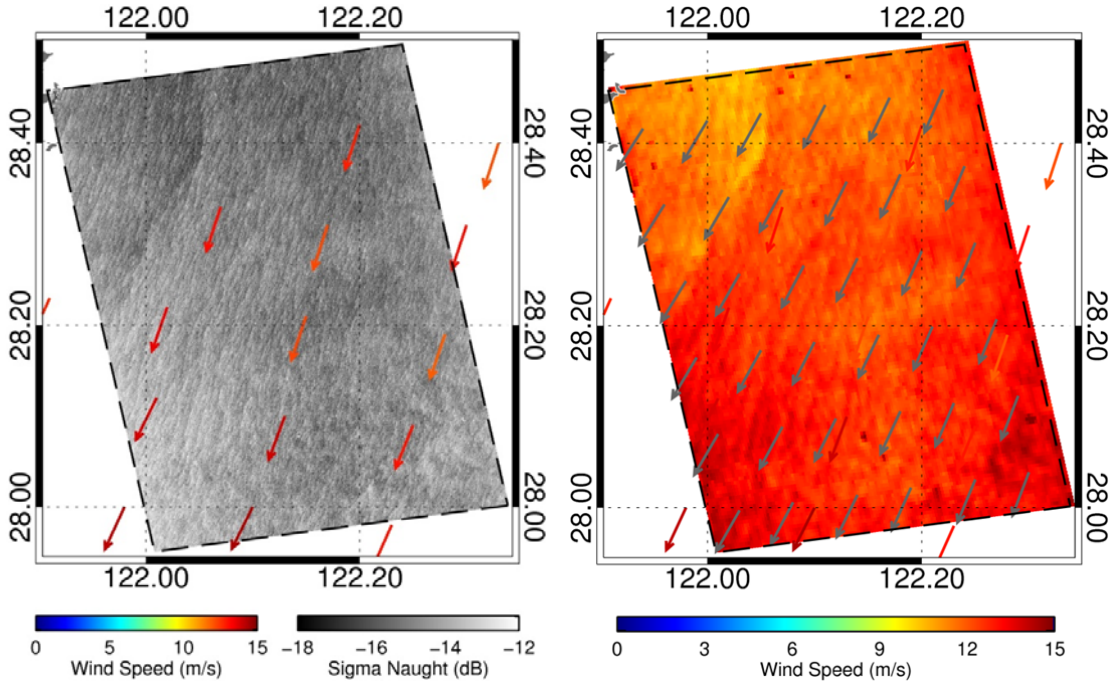

(a) *(b)*

Figure 5 (a) The calibrated TS-X ScanSAR image acquired at 9:51 UTC on February 25, 2009. The QuikSCAT wind field measurement at 9:52 UTC in the same day is overlaid. (b) Retrieved TS-X wind field using XMOD2 and the QuikSCAT wind field.

3. SOUTH CHINA SEA CAMPAIGN

During August and September in 2011, we carried out a campaign to validate the TS-X/TD-X retrieved sea surface wind field in the South China Sea (SCS). A large amount of TS-X/TD-X data in ScanSAR mode at VV polarization was ordered during August 24 to September 4, 2011. Fig. 6 shows position of R/V (DongFangHong 2, Ocean University of China) and acquisitions of the TS-X/TD-X data. Colourful rectangles indicate swath coverage of SAR data acquired during the campaign. The corresponding ship positions are also coloured. All the SAR images were ordered according to the planned course of the R/V. Two TS-X/TD-X data acquired on August 25 and 26, respectively, are near to positions of the R/V. However, due to severe weather caused by the super typhoon Nanmadol, the R/V had to adjust its ship course since Aug. 27, 2011. Consequently, the followed acquisitions of the SAR image were completed far away from the R/V. The pink and green rectangles show the TS-X acquired on Aug. 25 and the TD-X acquired on Aug. 26, respectively. Detailed information for the SAR acquisitions and shipborne measurements are given in Tab. 2.

Tab. 3: Detailed information for TS-X/TD-X and shipborne measurements during the SCS campaign

Case No.	SAR Sensor	SAR acquisition	Shipborne Pos.	Shipborne Time	Shipborne measurements
Case 1	TS-X	Aug.25, 2011 22:05 UTC	19.98°N 119.84°E	Aug.25, 2011 21:12 UTC	11.6 m/s 187° (going to)
Case 2	TD-X	Aug.26, 2011 10:07 UTC	19.99°N 118.43°E	Aug.26, 2011 09:55 UTC	7.5 m/s 199°(going to)

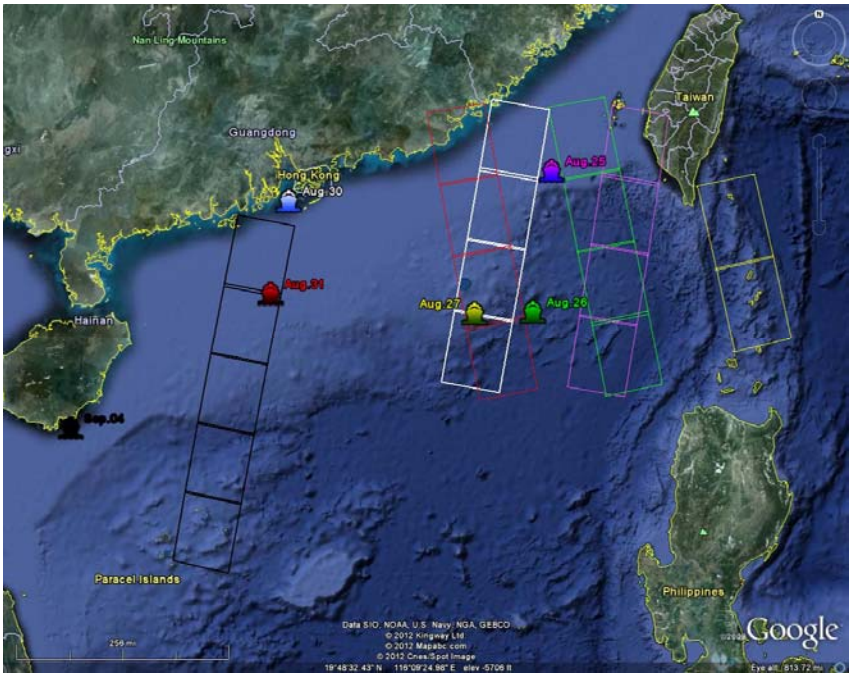

Figure 6. Acquisitions of TS-X/TD-X and positions of R/V DongFangHong 2 in the SCS campaign

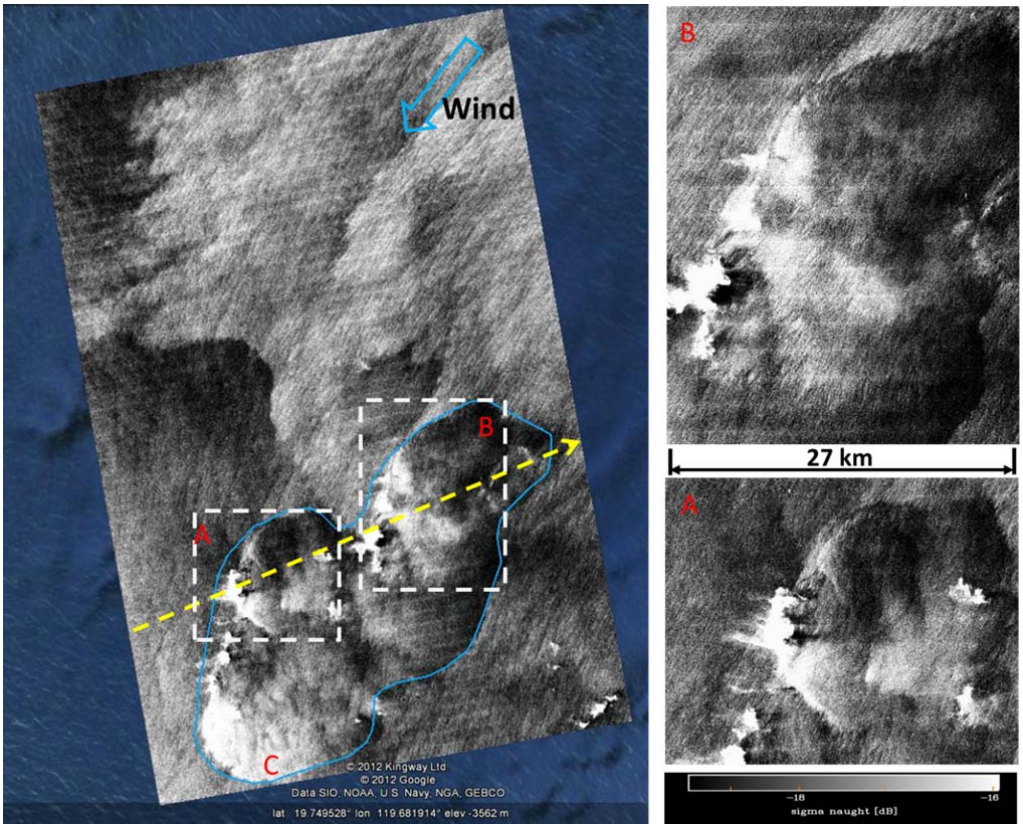

Figure 7. Quicklook of the TD-X ScanSAR image acquired on Aug. 26, 2011 at 10:07 UTC. Blue line encircles the area which is significantly affected by rain cell. Yellow line marks the selection used to analyse the radar backscatter variation through regions which are affected by rain cell. (map © Google earth)

After around 12 hours of the TS-X acquisition, the TD-X acquired another ScanSAR mode image covering a similar area as TS-X. Quicklook of the TD-X image superimposed on the map is shown in Fig.7. In the SAR imagery, the upright panel shows stronger sea surface backscatter than the lower left panel. It can be also noticed that the radar backscatter in the lower part of the image is significantly interfered. Rain rate measured by WindSat at 9:30 UTC in the same day as the TD-X data is shown in Fig. 9 (a). The maximum rain rate of 2.4 mm/h is in the cell which corresponds well to the region B shown in Fig.6. Therefore, we considered the area marked by blue line is significantly affected by rain cells. In the right panel of Fig.7, subscenes over region A and B are shown as well. One can observe that the two regions have similar structures of radar backscatter which changes from very bright "flash" points, to slight bright patches, then to dark pattern, from near range to far range.

Profile of the TS-X radar backscatter along the yellow dash line through region A and B is shown in Fig.8.

In a previous study, Melsheimer *et al.* [14] investigate effects of rain cell on SAR imagery using SIR-C/X-SAR data in multifrequency (L-, C-, and X-band) and multipolarization (HH, VV and HV). They summarized that the radar backscatter over ocean in the presence of rain cells is mainly associated with three processes: 1) scattering and attenuation of radar microwaves by hydrometeors in atmosphere, 2) the modification (enhancement or reduction) of sea surface roughness by rain drops, and 3) the enhanced sea surface roughness by wind gust. Although it is claimed [15] that the volume scattering of microwave by rain drops is not easy detectable in SAR imagery, we indeed observe that all the three processes in this TD-X image which was acquired over the typhoon-affected region.

In region B, we can observe that the radar backscatter increases sharply from -17.5 dB to -7.5 dB within a distance of ~ 2 km, which is very likely due to volume scattering of radar microwave from hydrometeors in atmosphere [16]. A small "shadow" area follows these flash points, where the radar backscatter decreases sharply to -22.5 dB. Then the radar backscatter gradually increases to -12.5 dB within a distance of ~ 8 km, which should attribute to the enhancement of sea surface roughness by ring waves [17] generated from rain drops. In this case, the Bragg wavelength lies between 2.23 cm and 2.33 cm, and the sea surface wind speed ranges between 4 m/s and 10 m/s in rain free area (referring to Fig. 9 (b)), which both are favourable conditions to increase the sea surface roughness by rain drops as shown in wave tank experiment [18]. Further to far range area in B, the large darker pattern is observed. As shown in Fig.13, the radar backscatter decreases from -12.5 dB till -25 dB spanning a distance of around 20 km. As shown in [14], the attenuation of radar microwave induced by hydrometeors occurs regardless of radar frequency. Therefore, the observed lower radar backscatter pattern in both region A and B are mostly due to the attenuation of radar microwave caused by hydrometeors in atmosphere. With respect to region C, the higher radar backscatter spreads radially into the downwind direction, while the slight dark radar backscatter lies in the opposite upwind direction. Therefore, we infer that the bright pattern C is induced by downward airflow (downdraft or gust front) produced by rain cells.

In the presence of rain cells, the sea surface wind retrieved from the TD-X data exhibits significantly variations, as shown in Fig.9 (b). Particularly due to the volume scattering, the retrieved wind speed is strongly interfered. In this section, effects of rain cells on X-band SAR radar backscatter is analysed based on a TD-X image acquired over a typhoon-effecting region. One may notice that the X-band SAR tends to be sensitive with rain fall, which can induce some interferes for sea surface wind field retrieval.

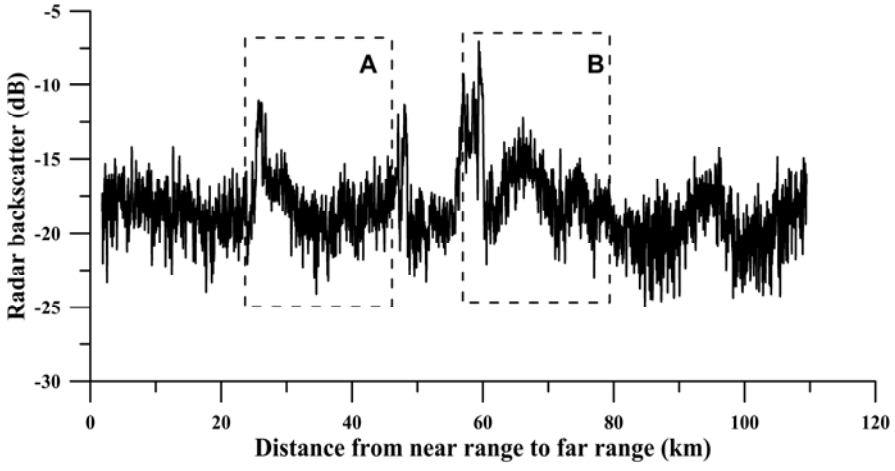

Fig. 8 Variations of TD-X radar backscatter along the yellow line shown in Fig. 7.

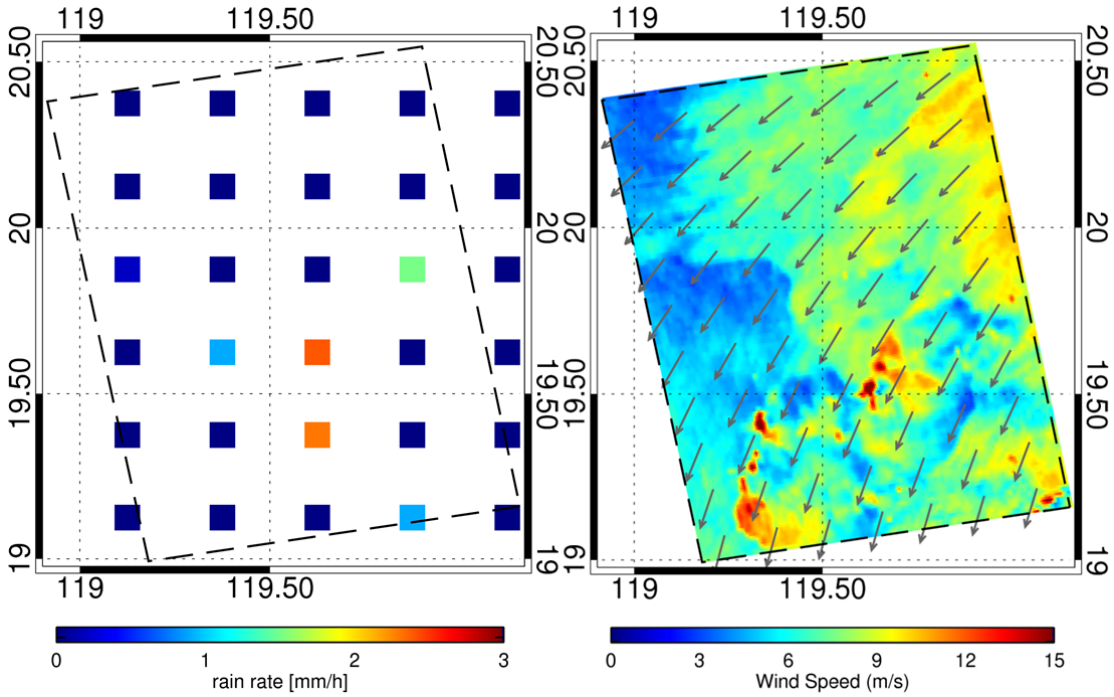

(a) *(b)*

Fig. 9 (a) Rainfall rate measured by WindSat at 9:30 UTC on Aug. 26, 2011. (b) Retrieved sea surface wind field retrieved from the TD-X data as shown in Fig. 7.

Although missing opportunity to compare the retrieved sea surface wind with in situ measurements due to an approaching typhoon, a pre-ordered TD-X image was acquired which images the typhoon Nanmadol over the Luson Strait, as indicated by the two yellow rectangles in Fig. 6. The calibrated TD-X ScanSAR image is shown in Fig. 10 (a). The dark patterns in the north-east and south-west of the image indicate attenuation of radar backscatter induced by strong rainfall of typhoon, which is, however, not the same as the rain effect in the case described above. The camiguin island is near to eye of the typhoon Nanmadol. The Mount Camiguin occupying the southwester tip of the island has an elevation of 712 metres. The large contrast between of backscatter in the north-west and south-east of the island indicates that orography of the island has an influence on the sea surface wind field. The retrieved sea surface wind field for this case using XMOD2 is shown in Fig. 10 (b). The retrieved wind field shows light wind speed in the eye is of around 5 m/s – 10 m/s. Away from the eye, the higher wind speed appears in eye wall area. In the south-east of the eye and north-west of the inner rain band, the sea surface wind speed is of around 25 m/s. However, we found a large area in the southwester of the eye, i.e., in front of the Camiguin island, which shows a higher wind speed above 30 m/s. Therefore, we infer that the significant asymmetric wind field structure in the eye wall area is closely related to the local orography.

In addition, attenuation of radar backscatter induced by heavy rain significantly deduces the retrieved sea surface wind speed to be lower than 2.5 m/s.

In this section, we present two examples of retrieved sea surface wind field from the TS-X/TD-X data acquired during the joint campaign in the SCS. One is to analyse rainfall effect on the X-band SAR image and its retrieved sea surface wind speed in detail. The other case is to demonstrate the newly developed XMOD2 also has capability to retrieve the sea surface wind field under typhoon conditions. Moreover, land effect on structure of typhoon wind field is also discussed.

4. CONCLUSION AND OUTLOOK

A new GMF called XMOD2 to retrieve the sea surface wind field from the X-band TS-X/TD-X is introduced in this paper. Compared to the previous XMOD1, XMOD2 relates nonlinearly the sea surface wind vector with radar backscatter in X-band SAR. The difference of upwind and downwind in the sea surface backscatter is depicted as well in the new GMF. Moreover, compared to XMOD1 which is suitable for moderate wind speed,

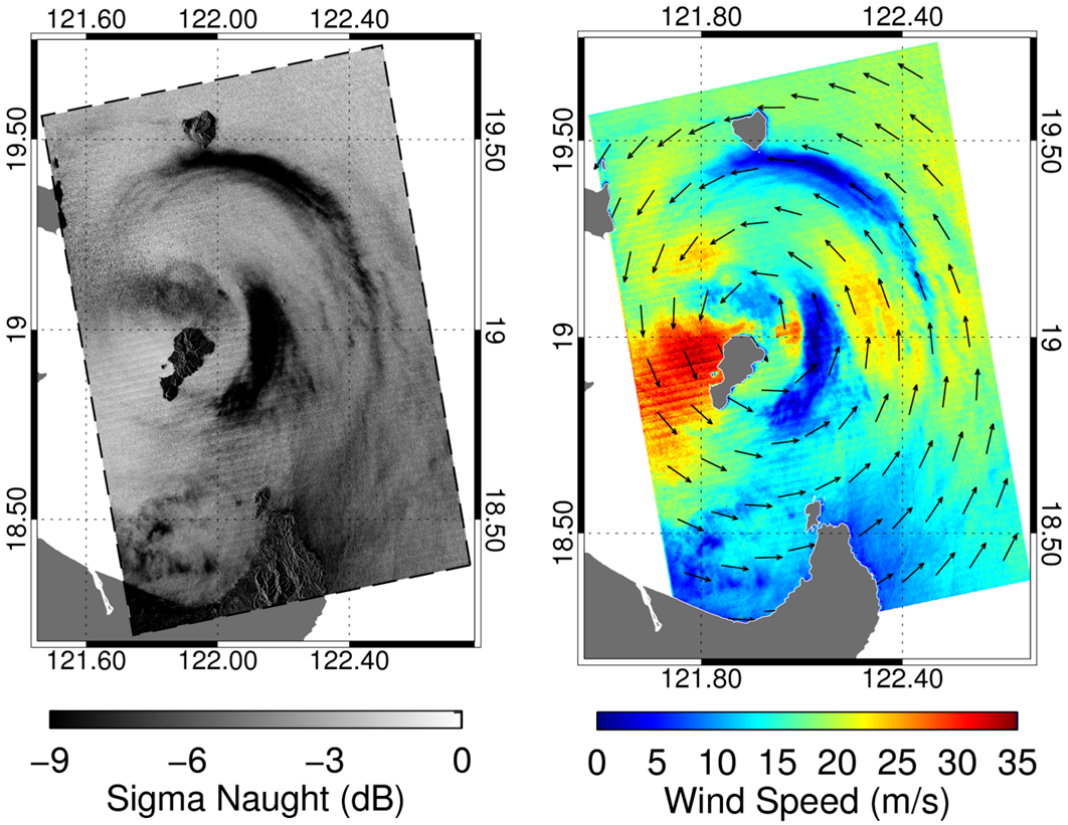

(a) *(b)*

Figure 10. (a) The TD-X ScanSAR image acquired over the typhoon Nanmadol in the Luson Strait on Aug. 27, 2011 at 09:49 UTC. (b) The retrieved sea surface wind field using XMOD2

the applicable wind speed retrieval by XMOD2 is extended to a wider range of 1 m/s to 25 m/s. The Bora event presented above shows that the new GMF also performs fairly well under high wind condition. The applicable incidence angle for wind field retrieval by XMOD2 is between 19° and 45°.

The comparison of retrieved sea surface wind speed from TS-X/TD-X data with *in situ* buoy measurements shows a good agreement with a bias of 0.39 m/s, an RMSE of 1.52 m/s and a SI of 16.3% are achieved for 371 collocations with buoy measurements. A case study for TS-X data acquired over the China coasts is collocated with QuikSCAT measurement for validation as well.

It is unfortunate that we lost an important opportunity to validate the XMOD2 by comparing to shipborne measurements conducted in the SCS campaign due to the severe typhoon. However, we acquired a TD-X data which shows the radar backscatter is significantly affected by rain cells brought by the tropical cyclone. Four radar backscatter features are identified. Among them, two features, i.e. volume scattering and attenuation are due to the interaction of radar microwave with hydrometeors in atmosphere. The other two are due to the surface roughness is modified by ring waves generated from rain drops and convective scale downdrafts on the rainfall. In addition, we also acquired a TD-X image over the typhoon Nanmadol in this campaign, which is an invaluable data for typhoon research using SAR. In the typhoon case, on the one hand, it shows that the XMOD2 is capable of retrieving the sea surface wind field under typhoon conditions. On the other hand, it also shows that the local orography should have a significant impact on the sea surface wind field.

Although the present validation shows that XMOD2 can yield a good estimation for sea surface wind speed, a large dataset is essential for further validation. We have tried to match the achieved TS-X/TD-X to ASCAT measurements, unfortunately, there is not one case meeting the searching criteria, thus we plan to expand acquisitions of TS-X/TD-X. However, it is found that

the WindSat measurements match very well with TS-X/TD-X data (such as presented in the case study in section V), which might be another validation dataset for future studies.

5. REFERENCES

[1] Stoffelen, A. & Anderson, D. (1997). Scatterometer data interpretation: Estimation and validation of the transfer function CMOD4. *J. Geophys. Res.*, **102**(C3), 5767-5780.

[2] Quilfen, Y., Chapron, B., Elfouhaily, T., Katsaros, K., & Tournadre, J. (1998). Observation of tropical cyclones by high-resolution scatterometry. *J. Geophys. Res.*, 103(C4), 7767–7786.

[3] Hersbach, H., Stoffelen, A., & de Haan, S. (2007). An Improved C-band scatterometer ocean geophysical model function: CMOD5. *J. Geophys. Res.*, **112**, C03006, doi:10.1029/2006JC003743.

[4] Stoffelen, A., & Anderson, D. (1997). Scatterometer Data Interpretation: Measurement Space and Inversion. *J. Atmos. Oceanic Technol.*, **14**(6), 1298–1313.

[5] Lehner, S., Horstmann, J., Koch, W., & Rosenthal, W. (1998). Mesoscale wind measurements using recalibrated ERS SAR images. *J. Geophys. Res.*, **103**(C4), pp. 7847–7856.

[6] Li, X.-F., Zheng, W., Pichel, W.G., Zou, C.-Z. & Clemente-Colon, P.C. (2007). Coastal katabatic winds imaged by SAR. *Geophys Res. Lett.*, **34**(L03804), doi:10.1029/2006GL028055.

[7] Signell, R. P., Chiggiato, J., Horstmann, J., Pullen, J., & Askari, F. (2010). High-resolution mapping of Bora winds in the northern Adriatic Sea using synthetic aperture radar. *J. Geophys. Res*, 115 (C04020), doi: 1029/2009JC005524.

[8] Li, X.-M., Li, X.-F., & He, M.-X. (2009). Coastal upwelling observed by multi-satellite sensors. *Sci. China Ser. D-Earth Sci.*, **52**(7), 1030-1038, doi: 10.1007/s11430-009-0088-x.

[9] Christiansen, M. B., & Hasager, C. B. (2005). Wake effects of large offshore wind farms identified from satellite SAR. *Remote Sens. Environ.*, **98**(2–3), 251-268.

[10] Ren, Y.-Z., Lehner, S., Brusch, S., Li, X.-M. & He. M.-X. (2012). An algorithm for the retrieval of sea surface wind fields using X-band TerraSAR-X data. *Int. J. Remote Sens.*, **33**(23), 7310–7336.

[11] Li, X.-M., & Lehner, S. (2012). Sea surface wind field by TerraSAR-X and Tandem-X data: Algorithm development. Submitted to *IEEE Geosci. Remote Sens.*

[12] Monaldo, F., Thompson, D., Pichel, W., & Clemente-Colon, P. (2994). A systematic comparison of QuikSCAT and SAR ocean surface wind speeds. *IEEE Trans. Geosci. Remote Sens.*, **42**(2), 283–291.

[13] Yang, X., Li, X., Pichel, W. G. & Li, Z. (2011). Comparison of ocean-surface winds retrieved from QuikSCAT scatterometer and RADARSAT-1 SAR in offshore waters of the US west coast. *IEEE Geosci. Remote Sens. Lett.*, 8(1), 163–167.

[14] Melsheimer, C., Alpers, W., & Gade, M. (1998) Investigation of multifrequency/multipolarization radar signatures of rain cells over the ocean using SIR-C/X-SAR data. *J. Geophys. Res.*, **103**, 18,851–18,866.

[15] Alpers, W., & Melsheimer, C. (2004). *"Rainfall,"* Synthetic Aperture Radar Marine Users Manual. Washington, DC: U.S. Dept. Commerce, NOAA, 353–372.

[16] Moore, R. K., Mogili, A., Fang, Y., Beh, B. & Ahamad, A. (1997). "Rain measurement with SIR-C/X-SAR," *Remote Sens. Environ.*, **59**(2), 280–293.

[17] Wetzel, L. B. (1990). On the theory of electromagnetic scattering from a raindrop splash. *Radio Sci.*, **25**, 1183–1197.

[18] Braun, N., Gade, M. & Lange, P. A. (2002). The effect of artificial rain on wave spectra and multi-polarization X band radar backscatter. *Intl. J. Remote Sens.*, **23**(20), 4302–4323.

ACKNOWLEDGMENTS

The TS-X/TD-X data are kindly provided by DLR via the AO proposal of OCE1044. We thank Dr. Thomas Bruns at DWD for providing the GSM model data. We especially thank Mr. Miguel Bruck for essential help on data ordering with in situ buoy measurements. The QuikSCAT and WindSat data are accessed from http://podaac.jpl.nasa.gov/ and www.ssmi.com, respectively. The project was also supported by the Open Research Fund (ID: 2010LDE01)of Key Laboratory of Digital Earth, Center for Earth Observation and Digital Earth, Chinese Academy of Sciences.